Check for updates

Bioevaluation of magnetic mesoporous silica rods: cytotoxicity, cell uptake and biodistribution in zebrafish and rodents†

Jan Grzelak, [ID] [a] Mariana Teles, [b] Nerea Roher, [ID] [b] Alba Grayston, [c] Anna Rosell, [c] Martí Gich*[a] and Anna Roig [ID] *[a]

Mesoporous silica nanoparticles (MSN) characterized by large surface area, pore volume, tunable chemistry, and biocompatibility have been widely studied in nanomedicine as imaging and therapeutic carriers. Most of these studies focused on spherical particles. In contrast, mesoporous silica rods (MSR) that are more challenging to prepare have been less investigated in terms of toxicity, cellular uptake, or biodistribution. Interestingly, previous studies showed that silica rods penetrate fibrous tissues or mucus layers more efficiently than their spherical counterparts. Recently, we reported the synthesis of MSR with distinct aspect ratios and validated their use in multiple imaging modalities by loading the pores with maghemite nanocrystals and functionalizing the silica surface with green and red fluorophores. Herein, based on an initial hypothesis of high liver accumulation of the MSR and a future vision that they could be used for early diagnosis or therapy in fibrotic liver diseases; the cytotoxicity and cellular uptake of MSR were assessed in zebrafish liver (ZFL) cells and the *in vivo* safety and biodistribution was investigated *via* fluorescence molecular imaging (FMI) and magnetic resonance imaging (MRI) employing zebrafish larvae and rodents. The selection of these animal models was prompted by the well-established fatty diet protocols inducing fibrotic liver in zebrafish or rodents that serve to investigate highly prevalent liver conditions such as non-alcoholic fatty liver disease (NAFLD). Our study demonstrated that magnetic MSR do not cause cytotoxicity in ZFL cells regardless of the rods' length and surface charge (for concentrations up to 50 µg ml^{-1}, 6 h) and that MSR are taken up by the ZFL cells in large amounts despite their length of ~1 µm. In zebrafish larvae, it was observed that they could be safely exposed to high MSR concentrations (up to 1 mg ml^{-1} for 96 h) and that the rods pass through the liver without causing toxicity. The high accumulation of MSR in rodents' livers at short post-injection times (20% of the administered dose) was confirmed by both FMI and MRI, highlighting the utility of the MSR for liver imaging by both techniques. Our results could open new avenues for the use of rod-shaped silica particles in the diagnosis of pathological liver conditions.

Introduction

Mesoporous silica nanoparticles (MSN) are solid materials that contain empty monodispersed channels in the mesoporous range (between 2 and 50 nm, according to the IUPAC classification).[1–3] MSN biosafety, large surface area, large pore volume, robustness, and the possibility of surface modification,[2,4,5] have made this system very attractive in biomedicine.

[a]Institut de Ciència de Materials de Barcelona (ICMAB-CSIC), Campus UAB, 08193 Bellaterra, Catalonia, Spain. E-mail: mgich@icmab.es; anna.roig@csic.es

[b]Institute of Biotechnology and Biomedicine (IBB), Universitat Autònoma de Barcelona, 08193 Barcelona, Spain

[c]Neurovascular Research Laboratory, Vall d'Hebron Research Institute (VHIR), 08035, Barcelona, Catalonia, Spain

† Electronic supplementary information (ESI) available. See DOI: https://doi.org/10.1039/d2ra05750f

Since the first report on mesoporous silica as a drug delivery system,[6] MSN have been studied extensively as therapeutic carriers.[7] Although MSN have not yet been approved for clinical trials, considerable progress has been made in designing and developing MSN-based agents for diagnostic[8,9] and/or therapeutic[2,10] purposes.

Worth noting is that the vast majority of research on silica materials focuses on spherical particles,[2,11–13] while not much attention has been given to anisotropic shapes, possibly due to the challenging fabrication of particles with well-controlled rod-like morphology. Although some studies on mesoporous silica nanorods (MSR) have been reported, this is still an emerging field. Available studies showed that the shape of silica particles could influence their biodistribution, major lung accumulation,[14,15] cellular uptake,[16–20] toxicity,[15,21] degradation,[14,15] drug release[22] or mobility,[23] but further knowledge is still necessary to evaluate how the rod shape could be a determinant factor in the context of

diseases lacking early-stage diagnostic tests or therapeutic strategies. A relevant example is non-alcoholic fatty liver disease (NAFLD), which is a major cause of liver conditions worldwide.[24–26] NAFLD progresses in approximately 10–20% of cases to non-alcoholic steatohepatitis (NASH), characterized by hepatocellular steatosis, inflammation, and fibrosis, and can lead to more severe and irreversible liver damage with fatal consequences.[27,28]

Pioneering studies reported that silica rods exhibit higher diffusivity than spheres in the intestinal mucus, leading to deeper penetration and longer retention time in the gastrointestinal tract.[29,30] The superior diffusivity of silica rods has been explained by rotational dynamics facilitated by the fibrous structure of mucosal tissue and shear flow. Besides, it is well known that rod-shaped pathogenic bacteria of the gastrointestinal tract are also highly mobile in mucus.[31] We hypothesize that similar behavior could occur with MSR in fibrotic liver tissue, and they could offer potential advantages over spherical particles in an early-stage diagnosis or therapeutic opportunities in the context of NAFLD and NASH. This work sets the basis for further studies in the abovementioned field by reporting on the *in vitro* cytotoxicity and cellular uptake of MSR in zebrafish liver (ZFL) cells and the *in vivo* biodistribution of the MSR in zebrafish larvae and rodents with already existing models of fibrotic liver.

Recently, we synthesized MSR with two distinct aspect ratios (~2 and ~5).[32] We equipped the MSR with multiple imaging modalities, loading the pores with magnetic nanoparticles and functionalizing their surface with fluorophores of two emission wavelengths. Here, by using magnetic measurements, fluorescence molecular imaging (FMI), and magnetic resonance imaging (MRI), we investigated the toxicity and biodistribution of the MSR in two *in vivo* preclinical models of different complexity. On the one hand, zebrafish (*Danio rerio*) is one of the simplest organisms with a liver, and zebrafish larvae can be used without ethical clearance. The larvae are transparent, and their liver is readily visible at low magnifications. Besides, well-established animal models of NAFLD can be induced in both larvae and adult zebrafish by a specific feeding protocol.[33–35] Uptake and toxicity *in vitro* studies were undertaken using ZFL while we studied toxicity and biodistribution in zebrafish larvae and rodents. Higher complexity rodent models are relevant because previous studies of murine exposure to high aspect ratio mesoporous silica reported accumulation in the lungs, with different levels of toxicity.[36] Still, other works concluded that rod-shaped mesoporous silica had good biocompatibility.[37] Due to the scarcity of studies on MSR and the variability of rod dimensions, animal models, doses and exposure times between the different experiments, more studies are needed to understand the relationship between the silica particle shape and toxicity in rodents. Our study shows low cytotoxicity and high liver accumulation of MSR in zebrafish larvae and rodents, setting the ground for further studies involving fibrotic liver models.

Materials and methods

Materials

MSR were synthesized using the following reagents. Hydrochloric acid (37%), poly(ethylene glycol)-*block*-poly(propylene glycol)-*block*-poly(ethylene glycol) (Pluronic P123), tetraethyl orthosilicate (TEOS), (3-aminopropyl)triethoxysilane (APTES), fluorescamine and triethylamine were purchased from Sigma-Aldrich and used as received. Ethanol was purchased from PanReac. Iron(III) nitrate nonahydrate was purchased from ACROS Organics and used as received. Cyanine5 NHS ester (Cy5-NHS) was purchased from Lumiprobe and used as received. The purity of all reagents was 98% or higher.

ZFL were cultured at 28 °C (optimal temperature for culturing zebrafish cells[38]), 5% CO_2 in Dulbecco's modified Eagle's medium (DMEM) with 4.5 g l^{-1} glucose, supplemented with 0.01 mg ml^{-1} insulin, 50 ng ml^{-1} EGF, 5% (v/v) antibiotic/antimycotic solution, 10% (v/v) heat-inactivated fetal bovine serum (FBS) and 0.5% (v/v) heat-inactivated trout serum (TS) as described in literature.[39] The MTT (3-(4,5-dimethylthiazol-2-yl)-2,5-diphenyltetrazolium bromide) substrate and DMSO were purchased from Sigma-Aldrich.

Synthesis and functionalization of silica rods

Extensive details on the synthesis and functionalization of the MSR used in this work have been previously reported.[32] Briefly, Pluronic P123 was dissolved in 1.7 M hydrochloric acid solution. After obtaining a homogeneous solution, the temperature was increased to 40 °C and the solution was stirred at 700 rpm. After 3 h, tetraethyl orthosilicate (TEOS) was added dropwise. Stirring was stopped after either 4 or 5 min, and the reaction was kept in static conditions for either 3 h or 24 h. After that, the reaction was kept at 80 °C for 24 h. Silica was then filtered and dried at 55 °C overnight. The surfactant was removed by washing the product in ethanol and the material was calcined in air at 550 °C for 5 h.

The rods were loaded with iron oxide nanoparticles (NPs) using a wet impregnation method, with iron(III) nitrate nonahydrate as the precursor. Impregnation was performed by heating the silica powder and the iron precursor at 60 °C, followed by a thermal treatment at 425 °C under an argon flow with 5% of hydrogen (v/v). Amine groups were grafted to the silica rods surface by APTES aminosilanization to enable the subsequent attachment of fluorophores. A stock solution of fluorescamine or Cyanine5 was added to an acetone dispersion of amino-functionalized MSR, leaving the mixture to react overnight. The particles were purified by washing three times with ethanol and centrifugation. Finally, the precipitate was dispersed in a small amount of acetone and dried in vacuum. The product was stored at 4 °C in the dark. Table 1 summarizes the physico-chemical characteristics and the labeling to identify the materials used in the present study.

Zebrafish liver cell viability studies

Cytotoxic of MSR on ZFL were assessed using the MTT assay. ZFL were cultured in 75 cm^2 cell culture flasks with vented caps (Falcon®). Confluent cells were lifted using 2 ml TrypLE Express (ThermoFisher) and seeded in 24 well plates (cells from one flask used for seeding in two plates) in complete medium, 500 μl per well. After 16 hours, the medium was changed to a minimal medium (0–0.5% FBS; 2% antibiotic/antimycotic). After 2 h of

Table 1 Physico-chemical characteristics of the materials used in these studies

Mesoporous silica rods (MSR)	Long rods (LR)	Short rods (SR)
Length (μm)	1.4 ± 0.3	0.9 ± 0.1
Width (μm)	0.3 ± 0.1	0.4 ± 0.1
Aspect ratio	4.7 ± 1.3	2.2 ± 0.5
Zeta potential (mV)	-38 ± 5	-34 ± 4
Rods loaded with Fe_2O_3 NPs	Fe_2O_3@LR	Fe_2O_3@SR
NP size (nm)	$7 \pm 3 \times 5 \pm 2$	$7 \pm 3 \times 5 \pm 2$
Crystallographic phase	Maghemite (100%)	Maghemite (100%)
Iron oxide content (wt%)	15 ± 1	15.0 ± 0.3
Saturation magnetization at 300 K (emu g^{-1} Fe_2O_3)	43 ± 4	42 ± 4
r_2 relaxivity (s^{-1} mM^{-1})	143 ± 14	108 ± 11
Rods loaded with Fe_2O_3 NPs and functionalized with amine groups	Fe_2O_3@LR-NH$_2$	Fe_2O_3@SR-NH$_2$
Zeta potential (mV)	33 ± 5	34 ± 5
Rods functionalized with fluorescamine	LR-FL	SR-FL
Emission wavelength (nm)	525	525
Rods loaded with Fe_2O_3 NPs and functionalized with Cy5	Fe_2O_3@LR-Cy5	Fe_2O_3@SR-Cy5
Emission wavelength (nm)	733	733

incubation, cell cultures were treated with MSR (Fe_2O_3@LR, Fe_2O_3@LR-NH$_2$, Fe_2O_3@SR, Fe_2O_3@SR-NH$_2$, each MSR type and condition in triplicate). Ten percent of culture medium volume was removed and replaced with the same volume of either water or stock solution of MSR, to obtain MSR concentrations of 0, 5, 20, 50 and 200 μg ml^{-1}. The cells were incubated with MSR for 6 h at 28 °C. Cells were then washed with PBS and the MTT substrate was added to 10% of the total volume and further incubated at 28 °C for 30 min. The solution was removed, the cells were solubilized in DMSO and the lysate absorbance was read on a Victor 3 plate reader (PerkinElmer) at 550 nm. The experiments compared two sets of materials on each plate (Fe_2O_3@LR with Fe_2O_3@SR, Fe_2O_3@LR with Fe_2O_3@LR-NH$_2$, Fe_2O_3@SR with Fe_2O_3@SR-NH$_2$, or Fe_2O_3@LR-NH with Fe_2O_3@SR-NH$_2$) in duplicates, and each type of material was assessed in 6 different experiments. The mean of control wells was set as 100% in each experiment.

Statistical analysis

Results are expressed as mean $\pm$ standard deviation (SD). Statistical analysis was done using GrahPad Prism (version 7.01 for Windows, GraphPad Software, San Diego, California USA, www.graphpad.com). The assumptions of normality and homogeneity of data were verified using the Shapiro–Wilk test. One-way analysis of variance (one-way ANOVA) was performed to assess significant differences among groups. When significant differences were found, the one-way ANOVA was followed by the post-hoc Tukey's test to signal significant differences between groups and to the control group. The significance of the results was ascertained at $p < 0.05$.

ZFL cell uptake studies

Before the exposure, the cells in culture were counted in a Neubauer chamber and 125 000 cells per well were seeded in 96 well plates. The cultures were incubated with MSR similarly as described for the MTT assay protocol. After 6 h, the cells were washed with PBS and centrifuged ($200 \times g$, 10 min at 4 °C). The uptake of MSR by ZFL was assessed using magnetometry measurements at 10 K. The cell pellets were collected from the wells and their magnetic moment measured by superconducting quantum interference magnetometer device (SQUID, Quantum Design Inc.) up to a maximum applied field of 60 kOe. The values of magnetic moment at remanence (*i.e.* at zero magnetic field after applying the maximum field) were divided by the number of cells calculated before the experiment. From previous measurements of the magnetization (magnetic moment per unit mass) of MSR samples recorded in the same conditions, it was possible to obtain the mass of MSR contained in each pellet. The number of uptaken particles per cell was determined from the relative content of Fe_2O_3 in Fe_2O_3@SR (15 wt% see Table 1), assessing the mass of a MSR of about 0.2 pg in the case of short rods. This mass, m, was calculated from the formula $m = (\rho \pi r^2 L)/(1 + \rho V_{total})$, where ρ is the density of silica (2.2 g cm^{-3}), r is the mean radius of the MSR, L is the mean length of the MSR, and V_{total} is the pore volume determined from nitrogen adsorption experiments.[40]

Evaluation of toxicity and biodistribution by fluorescence imaging in zebrafish larvae

Wild-type zebrafish (*Danio rerio*) were kept in a re-circulating aquarium with water temperature maintained between 26 and 28 °C. The lighting conditions were 14 : 10 h (light : dark) and adult fish were fed twice a day at a rate of 2% body weight, following a normal feeding protocol. Ammonia and nitrite levels were kept below the detection level at a pH between 6.8 and 7.5. The nitrate levels were maintained at <100 mg l^{-1}. For in-tank breeding, one female and three males were transferred to a breeding tank in the late afternoon. The divider was removed the next morning after the onset of light. Eggs were collected after 1–2 h and cultured in embryo medium (E3 medium) in a Petri dish (Deltalab). Fertilized eggs were separated from unfertilized eggs using a plastic pipette (Deltalab). The medium was changed every 24 h and, after hatching (approximately 3 days post-fertilization), the larvae were placed in a 96-well plate (ThermoFisher), one larva per well containing 200 μl of aquarium water with fluorescent MSR (functionalized with fluorescamine) at 0, 20, 50, 100, 200, 400 and 1000 μg ml^{-1}. For mortality studies, groups of larvae ($n \geq 5$ per condition) were used and monitored for 96 h using an optical microscope (Olympus). For uptake studies, groups of 4 larvae per condition

were used. After 24 h and 48 h of exposure, the uptake was confirmed by imaging the larvae using a fluorescence stereo-microscope (Nikon SMZ800) coupled with a camera (Nikon DS-Fi2) and a mercury lamp (Nikon C-LHGFI HG lamp, 130 W, wavelength range: 380–600 nm).

Fluorescence imaging in mice

Biodistribution studies by FMI were performed at the Preclinical Imaging Platform from VHIR (Barcelona). Ethical approval for the experiments was received by the Comité d'experimentació animal del Vall d'Hebron Institut de Recerca, protocol 70.18/10860.

FMI was performed to track the biodistribution of Fe_2O_3@SR-Cy5 in vivo and ex vivo using an IVIS® Lumina LT Series III imaging system (PerkinElmer, Waltham, MA). All images were acquired at the following $\lambda_{ex}/\lambda_{em}$ ranges: 625–655 nm/695–770 nm, centered at 640 nm/732 nm, respectively.

To study the in vivo/ex vivo biodistribution, C57BL/6JRj adult male mice (8 weeks of age) were injected via the tail vein with 200 μl of 3 mg ml^{-1} Fe_2O_3@SR-Cy5 dispersion in a D-mannitol aqueous solution (55 mg D-mannitol/ml H_2O). For the in vivo acquisitions, mice were anesthetized with isoflurane via facemask (5% for induction, 1.5% for maintenance in 95% O_2) and in vivo images in the dorsal and ventral views of the whole body were acquired at 30 min and 60 min post-injection. At the end of the scan, mice were euthanized by cervical dislocation under anesthesia and brain, heart, lungs, liver, spleen, and kidneys were dissected to measure the fluorescence of the principal organs ex vivo. A control animal was used as a background measurement both in vivo and ex vivo. Four out of five mice were successfully injected. There were problems with injecting one animal, therefore, this animal will not be considered in the following discussion.

For quantification, circular ROIs were manually drawn surrounding the fluorescence signal and total radiant efficiency (TRE; [photons per s]/[μW cm^{-2}]) was measured using the Living Image software (PerkinElmer, Waltham, MA) and corrected by the TRE from the corresponding ROI in the background control animal. For the in vivo analysis, abdominal ROIs were drawn on the ventral images due to the position of the organs of interest. For the ex vivo analysis, ROIs of each dissected organ were drawn in both dorsal and ventral positions, and the mean value was considered.

MRI imaging in rats

MRI in vivo experiments were performed in CIC BiomaGUNE (Donostia – San Sebastián) in the Singular Scientific and Technical Infrastructure (ICTS) of ReDIB-Molecular and Functional Imaging Facility. The animal license of the ICTS is AE-biomaGUNE-1116. Five female rats of RjHan:Sb type (9 weeks of age) were used in this study. Four rats treated with MSR and an untreated control animal were imaged for biodistribution studies.

Magnetic resonance imaging (MRI) in vivo experiments were performed at 7 T on a Bruker Biospec 70/30 equipped with a system of gradients of 12 cm interior diameter (400 mT m^{-1}) and connected to a console Bruker AVANCE III (300 MHz)

configured with 2 transmission channels and 4 reception channels. The experiments were carried out using a volumetric antenna of 72 mm in diameter with the transmission and reception of the signal optimized for the body of a rat. The animals were kept under anesthesia during the measurements using isoflurane (1–1.5%). The temperature of the animal was kept at approximately 37.0 °C through a system of hot air (SA instruments, NY, USA) and its respiration and temperature during the MRI image acquisition were monitored through a system SAII M1030 (SA instruments, NY, USA), which at the same time was used to synchronize the acquisition of images with the animal respiration. The monitoring was done at very short time intervals. The MRI session started with the acquisition of basal scans before the injection of MSR. For the injection, the MRI bed where the animal was located was taken out without changing the position of the animal and intravenous injection with 1.2 ml of dispersion of Fe_2O_3@SR (3 mg ml^{-1} in an aqueous solution of D-mannitol, 55 mg ml^{-1}) via the tail vein was performed. After the injection, the bed was introduced inside the scanner in the same position as before. The scans were repeated until acquiring the last scans at $t = 60$ min after the injection. For T_2 maps, MRI signal was measured at coronal planes using the sequence of Bruker MSME (multi slice multi-echo) with the following parameters: 20 echo times (TEs) within the interval TE = 7.5–150 ms, respiration synchronized with the acquisition, field-of-view (FOV) = 60×60 mm, ACQ matrix = 256×256, RECO matrix = 256×256, slice thickness = 1.5 mm, N slices = 8, averages = 2. For T_2^* maps, MRI signal was measured at axial planes using the sequence of Bruker MGE (Multi gradient echo) with the following parameters: 10 TEs within the interval TE = 3–39 ms, respiration synchronized with the acquisition, FOV = 60×60 mm, ACQ matrix = 256×192, RECO matrix = 256×256, slice thickness = 1.5 mm, N slices = 8, averages = 2.

After the MRI session, the animals were euthanized, perfused with a saline serum and their livers and lungs extracted. Organs of an untreated animal were also extracted and used as a control. The organs were frozen at -80 °C and freeze-dried in a LyoQuest-Telstar lyophilizer (0.05 mBar, 72 h). Then the organs were crushed and made into a homogeneous powder.

Magnetic hysteresis loops of the dried organ powders were collected at 10 K in a superconducting quantum interference magnetometer device (SQUID, Quantum Design Inc.) with a maximum applied field of 50 kOe.

The chemical analysis of the dry organs was made by inductively-coupled plasma and optical spectroscopies (ICP-OES). For this analysis, approximately 0.50 g of liver sample in duplicate or 0.05 g of lung sample in duplicate were digested with a mixture of concentrated HNO_3 and HF in a microwave oven (Milestone, Ultrawave model). The resulting digestions were introduced into an ICP-OES spectrometer (Agilent, model 5900), and the content of Fe and Si was determined.

Results and discussion

MSR of Santa Barbara Amorphous-15 (SBA-15) type were synthesized using a sol–gel method described in our previous

work.[32] Herein, we focus on the safety and biodistribution of rod-like silica particles of two distinct lengths (1.4 and 0.9 μm) and aspect ratios (AR = 4.7 and 2.2), denominated as long rods (LR) and short rods (SR) and with additional specific functionalizations. Namely, those rods were modified by growing superparamagnetic maghemite (γ-Fe_2O_3) nanocrystals within the pores (Fe_2O_3@LR, Fe_2O_3@SR). In a subsequent step, the rods were functionalized with amine (NH_2), rendering them with a positive surface charge (Fe_2O_3@LR-NH_2, Fe_2O_3@SR-NH_2), or further enabling the grafting of fluorophores (fluorescamine and Cyanine5) with emissions at λ = 525 and 730 nm respectively (Fe_2O_3@LR/SR-Cy5 and LR/SR-FL). Representative images of the two MSR systems are included in Fig. S1.†

Cytotoxicity and cell uptake studies in ZFL cells

Cell viability and cellular uptake assays were performed using ZFL cells (Fig. 1a). ZFL cell viability was studied using the MTT reduction assay (Fig. 1b) after exposing the cells for 6 h to long and short rods with negative and positive surface charges (Fe_2O_3@LR, Fe_2O_3@LR-NH_2, Fe_2O_3@SR, Fe_2O_3@SR-NH_2). It can be observed that none of the four MSR types caused cytotoxicity in ZFL cells for concentrations up to 50 μg ml^{-1}. At 200 μg ml^{-1}, viable cells decreased significantly for negatively (Fe_2O_3@LR) and positively charged (Fe_2O_3@LR-NH_2) long rods. The lowest toxicity in ZFL cells at 200 μg ml^{-1} was observed for positively charged short rods Fe_2O_3@SR-NH_2.

A relation between the aspect ratio of MSR and cytotoxicity has been reported in the literature.[17,21] However, this effect is complex and greatly depends on the cell type.[41,42] The cell viability assay results performed on ZFL cells indicate that the toxicity depends on the concentration and aspect ratio of MSR. At the same time, the surface charge does not have a significant effect on the studied conditions. Note that the MSR of AR = 2.2 (Fe_2O_3@SR, Fe_2O_3@SR-NH_2) induced less cytotoxicity in ZFL cells at 200 μg ml^{-1} than rods of AR = 4.7 (Fe_2O_3@LR, Fe_2O_3@LR-NH_2).
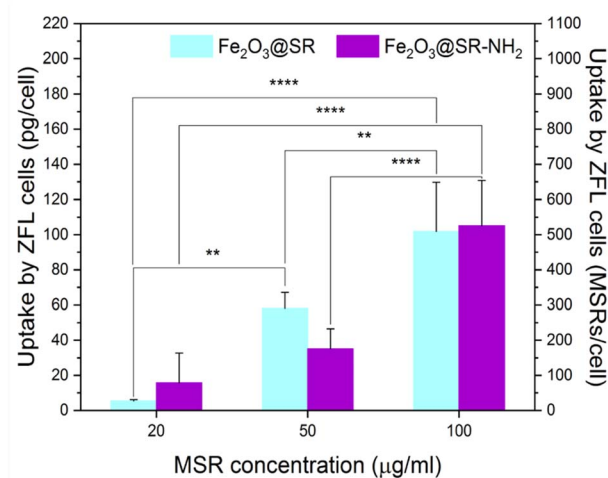

Fig. 2 Number of the MSR uptaken by ZFL cells presented as the mass of sample per cell (left axis) and number of MSR per cell (right axis). **$P \leq 0.01$, ****$P \leq 0.0001$.

The uptake of MSR by the ZFL cells was then studied by SQUID magnetometry at 10 K. Concentrations of the short rods (Fe_2O_3@SR, Fe_2O_3@SR-NH_2) up to 100 μg ml^{-1} were used for this experiment which we have considered the safest ones. The high sensitivity of the SQUID technique allows detecting very small magnetic moments. The remanent magnetic moment is proportional to the amount of the magnetic material and it is not affected by the diamagnetic signal from organic matter.[43] Fig. S2a and b† show a representative hysteresis loop of MSR and a ZFL cell pellet. The values calculated for each type of MSR are shown in Table S1† and depicted in Fig. 2. This method allowed us to calculate the uptake of MSR by ZFL cells and express it as the mass of the sample and an estimation of the number of uptaken rods per cell (see Methods section).

The uptake of MSR was concentration-dependent for both types of short rods. There were no significant differences in the
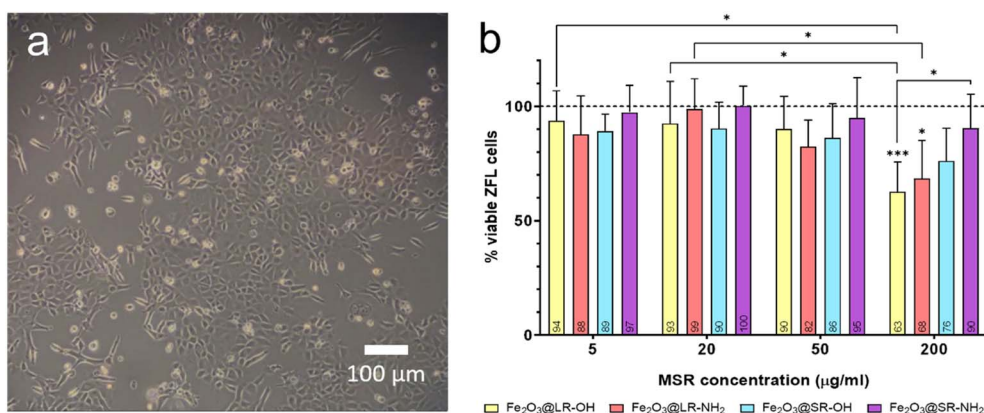

Fig. 1 (a) ZFL cells observed by an optical microscope, (b) ZFL cell viability after 6 h of exposure to the different types of MSR and four concentrations (n = 6 with technical replicates), plotted as mean + SD. The correspondence of p-values to the number of asterisks is the following: *$P \leq 0.05$, ***$P \leq 0.001$. The horizontal dotted line at 100% viable ZFL cells corresponds to the average number of viable cells of the control group, against which the viabilities were normalized. The asterisks above the bars represent statistically significant differences with respect to the control group.

© 2022 The Author(s). Published by the Royal Society of Chemistry

uptake between the negatively and positively charged rods. MSR were readily uptaken by the ZFL cells without inducing cytotoxicity despite a large number of internalized rods (>500 per cell) and their dimensions (average length 0.9 μm).

Biodistribution in zebrafish larvae and effects on survival

Zebrafish larvae were used as an intermediate model between *in vitro* studies and rodents *in vivo* experiments to study the uptake and toxicity of the MSR. The larvae were incubated with MSR functionalized with fluorescamine to visualize the rods inside the larvae using fluorescence microscopy.

Fig. S3a–d† shows the adult zebrafish and the stages between zebrafish eggs and larvae. The zebrafish eggs were collected and placed in E3 medium. Fertilized eggs were separated from unfertilized ones. After hatching, 3 days post-fertilization larvae were placed in a 96 well plate (1 larva per well) and incubated with a dispersion of fluorescamine-functionalized long and short rods (LR-FL and SR-FL). The toxicity of MSR on the larvae was monitored by observing the larvae in an optical microscope up to 96 h after exposure to various concentrations (20, 50, 100, 200, 400, and 1000 μg ml^{-1}; $n \geq 5$), 100% survival was observed at 96 h for each studied concentration (Fig. S3e†).

The uptake of MSR by zebrafish larvae was then studied in a fluorescence stereomicroscope. At 96 h of exposure, a strong green fluorescence of fluorescamine-functionalized rods was easily distinguishable from the larva autofluorescence, showing the nanoparticles' location in the liver and intestine (Fig. 3).

The evolution of MSR in the zebrafish larvae was tracked using the highest exposure concentration of 1000 μg ml^{-1}. After 24 h exposure, the larvae were observed in the fluorescence microscope and transferred to clean aquarium water. After an additional 24 h, the same larvae were observed. While at 24 h of exposure, MSR seemed to accumulate in the liver (Fig. 4b, e and

h), after the subsequent 24 h exposure (*i.e.*, after 48 h), it appeared that the fluorescence signal moved to the intestine (Fig. 4c, f and i).

Globally, the experiments on zebrafish larvae suggest that MSR pass through the liver of the larvae without causing toxicity, even when exposed to concentrations as high as 1000 μg ml^{-1}. This sets the ground for the future use of MSR in zebrafish fed with a high-fat diet as a fatty liver disease model.[33,44]

Fluorescence imaging studies in mice

The biodistribution of MSR in rodents after intravenous injection was studied by FMI and MRI. For these experiments, we selected the short magnetic rods, which had the lowest toxicity in the cell studies. Cyanine5-labeled short rods with iron oxide NPs (Fe$_2$O$_3$@SR-Cy5) were used in FMI studies performed on C57BL/6JRj mice. A clear fluorescence signal was observed at 30 min in the abdominal area of animals 1, 2 and 4 (Fig. S4a†) and remained relatively unchanged at 60 min (Fig. S4b†). At 60 min, fluorescence was also observed in the abdomen of animal 3. The quantitative analysis of fluorescence intensity (table included as Fig. S4c†) in the abdomen has shown similar fluorescence values in the first three animals at 30 min, and a slight decrease of these values was observed at 60 min.

After imaging at 60 min, the mice were sacrificed and the major organs (brain, lungs, liver, spleen, and kidneys) were extracted. The fluorescence images of the organs of treated animals were compared with control (Fig. 5a) and fluorescence intensity was quantified (Fig. 5b). As expected, high fluorescence was observed in the livers and similar intensity in the spleen and kidneys. No fluorescence was observed in the brains. In contrast to the results of biodistribution studies of MRI imaged rats (see next section), the fluorescence studies also indicate accumulation of MSR in the lungs.
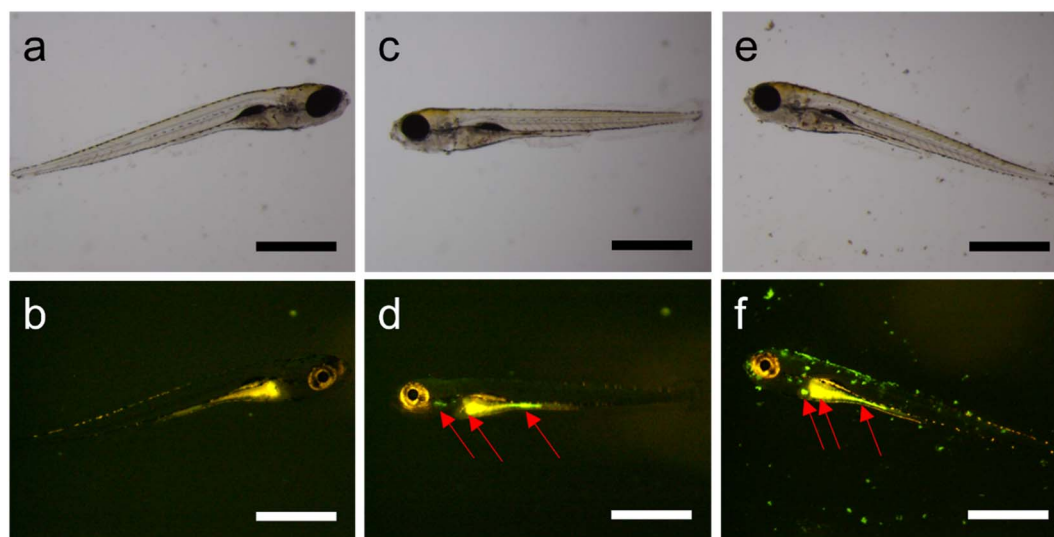

Fig. 3 MSR uptake by zebrafish larvae. Bright-field microscopy images (top) and corresponding fluorescence images (bottom) of an untreated larva (a) and (b) and two distinct representative larvae incubated with LR-FL (1 mg ml^{-1}) for 96 h (c)−(f). Red arrows mark the fluorescence from MSR. Scale bars: 1 mm.
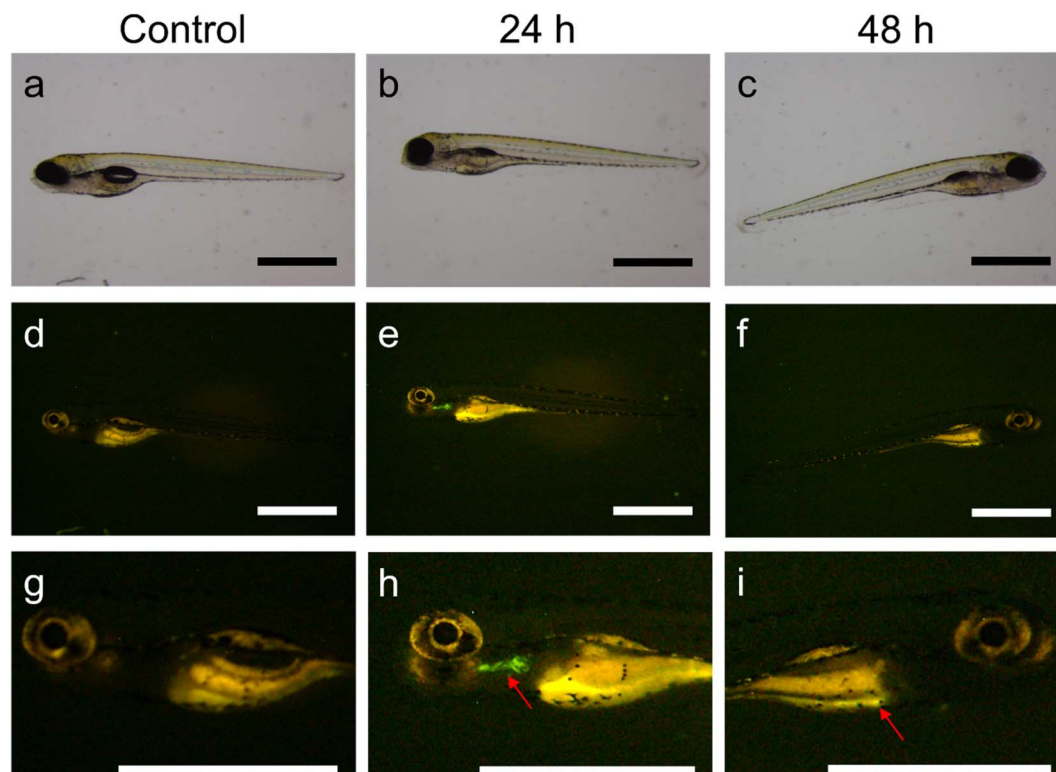
Fig. 4 Evolution of MSR uptake in zebrafish larvae. Bright–field optical microscopy images of an untreated larva (a) and a larva treated with LR-FL at 1000 μg ml^{-1} (b) and (c). Corresponding fluorescence images after 24 h (d) and (e) and 48 h (f). Corresponding high magnification images showing regions of interest (g), (h) and (i). Scale bars: 1 mm. Fluorescence from MSR is indicated with arrows.

MRI studies in rats

The magnetic MSR were further used as MRI T_2 contrast agents in experiments on rats. Four rats were injected with a dispersion of Fe$_2$O$_3$@SR (3 mg ml^{-1} in D-mannitol, 1.2 ml) and the MRI T_2 contrast was observed until 60 min post-injection. MRI scans were performed in coronal and axial planes. T_2 relaxation time maps recorded in coronal planes for two studied rats are shown in Fig. S5a–f.† Slices in which the liver covers the most extensive area were selected and compared. The coronal MRI T_2 images did not show a significant contrast change throughout the experiment. These findings are confirmed by the T_2 relaxation

time values (Fig. S5g†). Due to the characteristics of the lungs, changes in MRI T_2-contrast in this organ cannot be easily seen. Therefore, the potential pulmonary involvement was assessed indirectly by monitoring the animal respiration rate. During the acquisition of MRI scans, no critical changes in animal respiration or body temperature have been observed (Fig. S5h†). All four animals survived the experiment.

T_2^* relaxation time maps recorded in axial planes are shown in Fig. 6a–f. Similar to the T_2 maps, slices with the largest area occupied by the liver were analyzed. It can be seen that after the injection of MSR, the contrast in the liver decreases. The maps
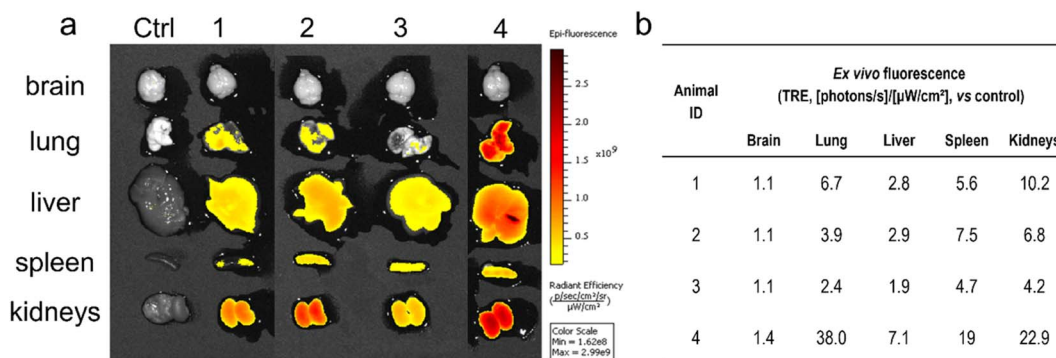

Fig. 5 (a) Ex vivo fluorescent images of organs extracted from mice treated with Fe$_2$O$_3$@SR-Cy5, (b) fluorescence values measured in the major organs.
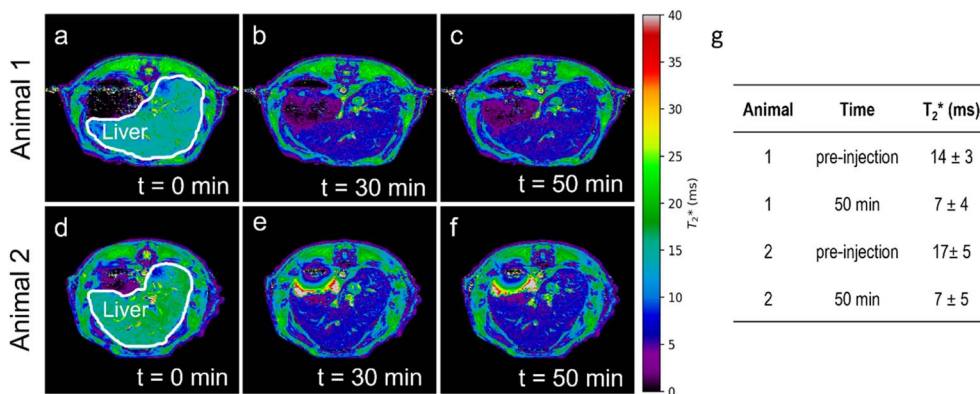
Fig. 6 T_2^* relaxation time maps of the abdominal area of (a)–(c) animal 1 and (d)–(f) animal 2 recorded at various times: $t = 0$ (pre-injection), $t = 30$ min and $t = 50$ min post-injection of Fe_2O_3@SR, (g) T_2^* values in the liver of the two studied rats, before and 50 min after MSR injection.

have been used to determine the T_2^* values in the liver (Fig. 6g). The results indicate a two-fold decrease of the MRI T_2^* contrast in the liver for both animals. We thus conclude that T_2^* sequences of axial planes were more effective in imaging the liver with the Fe_2O_3@SR. Furthermore, considering the better relaxivity value for the Fe_2O_3@LR,[32] this system should also be investigated in the future now that it is proved that the rats did not show adverse effects under the administration of SR.

Ex vivo MSR quantification

Following the scans, the animals were sacrificed and the major organs of interest were extracted to confirm the high accumulation of MSR in the liver and assess the involvement in the lungs that could not be observed by MRI. Livers and lungs were lyophilized and made into a homogeneous powder (Fig. 7a–d). A

quantitative biodistribution of magnetic rods was obtained by SQUID magnetometry and ICP-OES. Magnetization *vs.* magnetic field measurements of liver and lung samples of control and treated animals were measured at 10 K. Fig. 7e–f shows the data corresponding to half loop measurements (sufficient for our purposes) after correcting the diamagnetic contribution. The organs of both treated animals displayed similar magnetization curves. In the case of livers, a small magnetic remanence was observed for the control animal, and this value was subtracted from the M_r measured for the livers of treated animals.

The remanence values and the MSR content in the organs calculated from the remanent magnetization of Fe_2O_3@SR ($M_r = 3.3$ emu g^{-1}) are listed in Table 2.

The results were compared with data obtained from ICP-OES, where the amount of iron and silicon in liver and lung
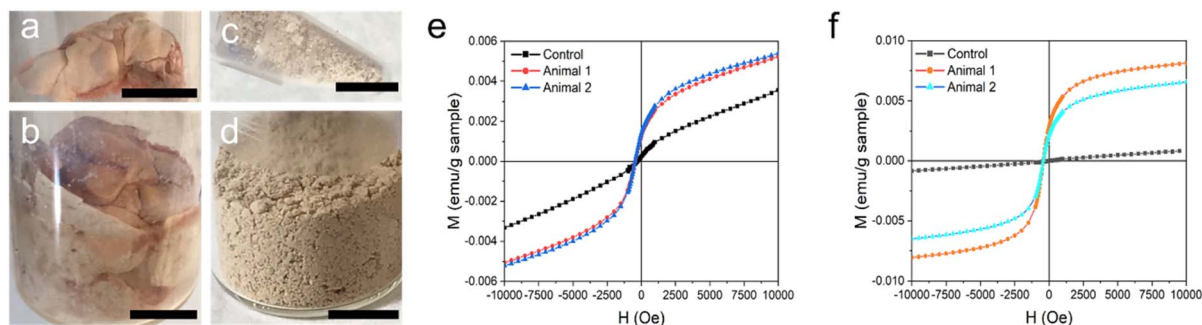

Fig. 7 Lyophilized organs of rats: (a) lungs and (b) liver. Homogenized samples of (c) lungs and (d) liver. Scale bars: 1 cm. Magnetic hysteresis loops at 10 K were recorded for (e) livers and (f) lungs.

Table 2 Fe_2O_3@SR quantification by SQUID in livers and lungs of rats, 60 min after administration

Organ	M_r (10^{-3} emu g^{-1} sample)	Total organ mass (g)	Total m_r of the organ (10^{-3} emu)	MSR mass in the organ (mg)
Liver 1	1.00	2.18	2.18	0.66
Liver 2	1.15	2.15	2.47	0.75
Lungs 1	2.86	0.23	0.66	0.20
Lungs 2	2.14	0.24	0.51	0.16

Table 3 Fe_2O_3@SR quantification by ICP-OES analysis of Fe and Si in livers and lungs of control (CT) and treated (1, 2) rats

Organ	Total organ mass (mg)	Fe content (mg g^{-1})	Si content (mg g^{-1})	Total Fe (mg)	Total Si (mg)
Liver CT	1927	0.57	<0.01	1.10	0.02
Liver 1	2182	0.50	0.16	1.10	0.35
Liver 2	2152	0.58	0.13	1.25	0.28
Lungs CT	232	0.09	<0.05	0.02	0.01
Lungs 1	230	0.29	0.30	0.07	0.07
Lungs 2	244	0.26	0.12	0.06	0.03

samples of control and treated animals were measured (Table 3). The quantification of iron using this method was not possible for liver samples due to the endogenous iron present in the liver, as seen from the control organ. Endogenous iron was also found in the lungs, although in smaller quantities.

The total mass of MSR sample in the organs was then calculated from ICP-OES, assuming 10.5 wt% iron in Fe_2O_3@SR and similarly, 39.8 wt% of silicon. The total amount of rods in

Fig. 8 Biodistribution in livers and lungs calculated from SQUID and ICP-OES data.

the organs calculated from Fe and Si analysis by ICP-OES was then compared with data derived from SQUID measurements (Fig. 8). The total mass of MSR injected in each animal was 3.6 mg.

The results of MSR quantification by SQUID are in good agreement with those derived from Si elemental analysis. Both techniques indicate *circa* five-fold higher uptake by the liver compared to the lungs. Moreover, approximately 20% of the injected sample accumulated in the liver 60 min after administration. Accumulation in these organs was compared with other results reported in the literature for different MSN (Table 4). For comparison, the accumulation was expressed in % of injected dose per gram of tissue (% ID per g tissue).

Our liver accumulation values are comparable to those of ref. 45 and 46, while longer times are related to higher liver accumulation. Regarding lungs, the results seem to indicate that for the smallest particle size or the shortest post-injection times, ref. 37 and 45, the highest lung accumulation occurs. However, the results can not be easily compared due to the differences in time post-injection, the animal model used, and the size of the particles. More experiments at longer exposure times and a systematic study for different MSR sizes and aspect ratios are needed to establish optimal features for an increased liver accumulation.

Conclusions

We have studied the *in vitro* cytotoxicity and *in vivo* safety and biodistribution of MSR with 1.4 and 0.9 μm in length, distinct aspect ratios (LR, AR = 4.7 and SR, AR = 2.2) and different surface charges, functionalized with magnetic nanoparticles and fluorophores (fluorescamine and Cyanine5). Studies carried out on ZFL cells showed no toxicity at 6 h for concentrations up to 50 μg ml^{-1} of both long and short rods, negatively and positively charged. At 200 μg ml^{-1}, the toxicity was significantly higher for long rods and still very low for both types of short rods. We observed that the rod's surface charge does not significantly affect cytotoxicity for this cell type. The uptake of MSR by ZFL cells was found to be concentration-dependent and similar for negatively and positively charged rods. The results indicate that despite its dimensions, a large number of rods
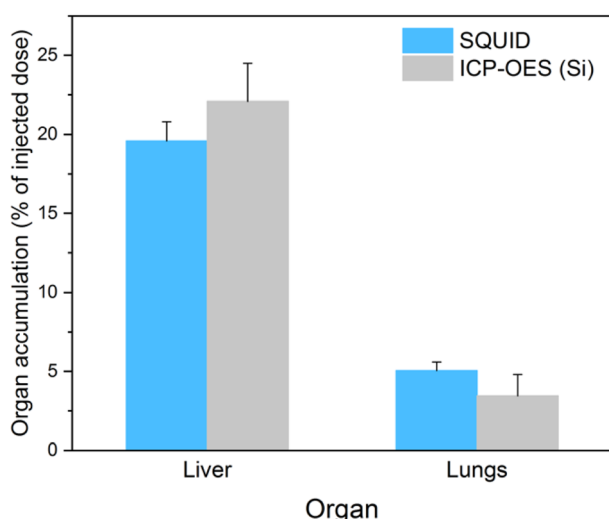
Table 4 Comparison of the liver and lung accumulation of MSR. The accumulation of MSR expressed in % of injected dose per g of tissue is the mean of the values calculated by the SQUID and ICP-OES techniques

Source	Material	Dimensions (nm)	Time post-injection (h)	Liver accumulation (% ID per g tissue)	Lung accumulation (% ID per g tissue)
This work	MSR loaded with Fe_2O_3 NPs	400 × 900	1	10 ± 1	18 ± 5
Ref. 45	MS spheres	120	0.5	17 ± 3	147 ± 37
			2	11 ± 3	140 ± 52
	MSR	136 × 1028	0.5	19.0 ± 5.0	132 ± 23
			2	21.4 ± 7.7	6 ± 2
Ref. 37	MSR	150 × 250	3	45.0 ± 5.0	18 ± 3
	MSR	150 × 450	3	41.0 ± 5.0	18 ± 4
Ref. 46	MS, almost spherical	900	1	18 ± 3	12 ± 0.1
Ref. 47	Porous silicon discoidal particles	400 × 1000	4	26 ± 2	17 ± 3

(>500) and up to 100 pg per cell were uptaken by the ZFL cells. *In vivo* studies on zebrafish larvae showed no toxicity at concentrations up to 1 mg ml^{-1} for 96 h exposure time. Interestingly, fluorescence in the larvae liver was observed at 24 h, while at 48 h the fluorescence came from the intestinal area. These results open the door to evaluate further the diagnostic and therapeutic potential of MSR for fibrotic liver using a zebrafish model fed with a high-fat diet. Fluorescence imaging was performed *in vivo* in mice after intravenous injection of Cyanine5-functionalized magnetic short rods (Fe$_2$O$_3$@SR-Cy5). Bright fluorescence was observed in the abdomen at 30 min and 60 min post-injection. Importantly, *ex vivo* imaging of the major organs showed a substantial accumulation in the liver, confirming our initial hypothesis. However, the accumulation in mice's lungs and particularly kidneys, not observed in rats, deserves further studies. MRI studies were performed on rats after intravenous injection with Fe$_2$O$_3$@SR. A decrease of MRI T$_2^*$ signal in the axial plane was seen at 30 min and 60 min in the liver, corroborating a high accumulation in the liver. The injection did not cause any abnormal respiration in the animals. Biodistribution studies of extracted organs also confirmed liver accumulation. The MSR content in the liver and lungs was quantified by SQUID magnetometry and ICP-OES elemental analysis leading to similar estimates. Data show that 20% of MSR were found in the liver, approximately five times more than in the lungs. The observed low toxicity, cellular uptake, and significant liver accumulation of the multifunctional MSR highlight their potential use for their future evaluation in some liver diseases, such as NAFLD. Studies using fatty liver animal models should be performed to determine whether rods can accumulate more efficiently in fatty or fibrotic liver tissue than their spherical counterparts.

Ethical statement

Fluorescence imaging in mice were performed at the Preclinical Imaging Platform from VHIR (Barcelona). All mice procedures were performed in accordance with the Guidelines for Care and Use of Laboratory Animals of VHIR. Ethical approval for the experiments was received by the Comité d'experimentació animal del Vall d'Hebron Institut de Recerca, protocol 70.18/10860. MRI experiments in rats were performed in CIC BiomaGUNE (Donostia – San Sebastián) within the Singular Scientific and Technical Infrastructure (ICTS) of ReDIB-Molecular and Functional Imaging Facility. Animal procedures were performed in accordance with the Guidelines for Care and Use of Laboratory Animals of ReDIB-Molecular and Functional Imaging Facility. The animal license of the ICTS is AE-biomaGUNE-1116.

Author contributions

Jan Grzelak: methodology, validation, formal analysis, investigation, visualization, writing-original draft, writing-review and editing. Mariana Teles: investigation, formal analysis, writing-review and editing. Nerea Roher: resources, investigation, formal analysis, writing-review and editing. Alba Grayston: investigation, formal analysis, writing-review and editing. Anna Rosell: resources, investigation, formal analysis, writing-review and editing. Martí Gich: conceptualization, formal analysis, resources, funding acquisition, supervision, writing-original draft, writing-review and editing. Anna Roig: conceptualization, formal analysis, resources, funding acquisition, supervision, writing-original draft, writing-review and editing.

Conflicts of interest

There are no conflicts to declare.

Acknowledgements

Notes and references

1 J. L. Vivero-Escoto, I. I. Slowing, V. S.-Y. Lin and B. G. Trewyn, *Small*, 2010, **6**, 1952–1967.
2 M. Manzano and M. Vallet-Regí, *Adv. Funct. Mater.*, 2020, **30**, 3–5.
3 R. Narayan, U. Y. Nayak, A. M. Raichur and S. Garg, *Pharmaceutics*, 2018, **10**, 1–49.
4 T. Yanagisawa, T. Shimizu, K. Kuroda and C. Kato, *Bull. Chem. Soc. Jpn.*, 1990, **63**, 988–992.
5 C. T. Kresge, M. E. Leonowicz, W. J. Roth, J. C. Vartuli and J. S. Beck, *Nature*, 1992, **359**, 710–712.
6 M. Vallet-Regi, A. Rámila, R. P. Del Real and J. Pérez-Pariente, *Chem. Mater.*, 2001, **13**, 308–311.
7 J. Key and J. F. Leary, *Int. J. Nanomed.*, 2014, **9**, 711–726.

8 X. Wang, H. Chen, Y. Zheng, M. Ma, Y. Chen, K. Zhang, D. Zeng and J. Shi, *Biomaterials*, 2013, **34**, 2057–2068.

9 E. Li, Y. Yang, G. Hao, X. Yi, S. Zhang, Y. Pan, B. Xing and M. Gao, *Nanotheranostics*, 2018, **2**, 233–242.

10 Q. Xu, Y. Yang, J. Lu, Y. Lin, S. Feng, X. Luo, D. Di, S. Wang and Q. Zhao, *Coord. Chem. Rev.*, 2022, **469**, 214687.

11 K. Shiba, N. Shimura and M. Ogawa, *J. Nanosci. Nanotechnol.*, 2013, **13**, 2483–2494.

12 R. R. Castillo, D. Lozano and M. Vallet-Regí, *Pharmaceutics*, 2020, **12**, 432.

13 R. K. Singh, K. D. Patel, C. Mahapatra, S. P. Parthiban, T. H. Kim and H. W. Kim, *ACS Appl. Mater. Interfaces*, 2019, **11**, 288–299.

14 X. Huang, L. Li, T. Liu, N. Hao, H. Liu, D. Chen and F. Tang, *ACS Nano*, 2011, **5**, 5390–5399.

15 L. Li, T. Liu, C. Fu, L. Tan, X. Meng and H. Liu, *Nanomedicine*, 2015, **11**, 1915–1924.

16 X. Huang, X. Teng, D. Chen, F. Tang and J. He, *Biomaterials*, 2010, **31**, 438–448.

17 D. Sen Karaman, D. Desai, R. Senthilkumar, E. M. Johansson, N. Råtts, M. Odén, J. E. Eriksson, C. Sahlgren, D. M. Toivola and J. M. Rosenholm, *Nanoscale Res. Lett.*, 2012, **7**, 358.

18 R. Vácha, F. J. Martinez-Veracoechea and D. Frenkel, *Nano Lett.*, 2011, **11**, 5391–5395.

19 H. Meng, S. Yang, Z. Li, T. Xia, J. Chen, Z. Ji, H. Zhang, X. Wang, S. Lin, C. Huang, Z. H. Zhou, J. I. Zink and A. E. Nel, *ACS Nano*, 2011, **5**, 4434–4447.

20 N. Hao, L. Li, Q. Zhang, X. Huang, X. Meng, Y. Zhang, D. Chen, F. Tang and L. Li, *Microporous Mesoporous Mater.*, 2012, **162**, 14–23.

21 T. Yu, A. Malugin and H. Ghandehari, *ACS Nano*, 2011, **5**, 5717–5728.

22 L. Li, X. Huang, T. Liu, H. Liu, N. Hao, D. Chen, Y. Zhang, L. Li and F. Tang, *J. Nanosci. Nanotechnol.*, 2012, **12**, 4458–4466.

23 R. Mestre, N. Cadefau, A. C. Hortelão, J. Grzelak, M. Gich, A. Roig and S. Sánchez, *ChemNanoMat*, 2021, **7**, 134–140.

24 Z. Younossi, A. B. Koenig, D. Abdelatif, Y. Fazel, L. Henry and M. Wymer, *Hepatology*, 2016, **64**, 73–84.

25 A. J. Sanyal, *Nat. Rev. Gastroenterol. Hepatol.*, 2019, **16**, 377–386.

26 D. Ferguson and B. N. Finck, *Nat. Rev. Endocrinol.*, 2021, **17**, 484–495.

27 A. Wree, L. Broderick, A. Canbay, H. M. Hoffman and A. E. Feldstein, *Nat. Rev. Gastroenterol. Hepatol.*, 2013, **10**, 627–636.

28 K. Gariani, D. Ryu, K. J. Menzies, H.-S. Yi, S. Stein, H. Zhang, A. Perino, V. Lemos, E. Katsyuba, P. Jha, S. Vijgen, L. Rubbia-Brandt, Y. K. Kim, J. T. Kim, K. S. Kim, M. Shong, K. Schoonjans and J. Auwerx, *J. Hepatol.*, 2017, **66**, 132–141.

29 M. Yu, J. Wang, Y. Yang, C. Zhu, Q. Su, S. Guo, J. Sun, Y. Gan, X. Shi and H. Gao, *Nano Lett.*, 2016, **16**, 7176–7182.

30 W. Liu, L. Zhang, Z. Dong, K. Liu, H. He, Y. Lu, W. Wu and J. Qi, *Nano Res.*, 2022, **15**, 9243–9252.

31 L. K. Sycuro, Z. Pincus, K. D. Gutierrez, J. Biboy, C. A. Stern, W. Vollmer and N. R. Salama, *Cell*, 2010, **141**, 822–833.

32 J. Grzelak, J. Gázquez, A. Grayston, M. Teles, F. Herranz, N. Roher, A. Rosell, A. Roig and M. Gich, *ACS Appl. Nano Mater.*, 2022, **5**, 2113–2125.

33 B. Chen, Y. M. Zheng, M. Q. Zhang, Y. Han, J. P. Zhang and C.-Q. Hu, *Front. Pharmacol.*, 2019, **10**, 1504.

34 A. Shwartz, W. Goessling and C. Yin, *Front. Immunol.*, 2019, **10**, 2840.

35 L. Yu, L. Gong, C. Wang, N. Hu, Y. Tang, L. Zheng, X. Dai and Y. Li, *Drug Des., Dev. Ther.*, 2020, **14**, 1493–1506.

36 T. Yu, K. Greish, L. D. McGill, A. Ray and H. Ghandehari, *ACS Nano*, 2012, **6**, 2289–2301.

37 D. Shao, M. Lu, Y. Zhao, F. Zhang, Y. Tan, X. Zheng, Y. Pan, X. Xiao, Z. Wang, W. Dong, J. Li and L. Chen, *Acta Biomater.*, 2017, **49**, 531–540.

38 S. Choorapoikayil, J. Overvoorde and J. Den Hertog, *Zebrafish*, 2013, **10**, 316–325.

39 D. Torrealba, D. Parra, J. Seras-Franzoso, E. Vallejos-Vidal, D. Yero, I. Gibert, A. Villaverde, E. Garcia-Fruitós and N. Roher, *Biomaterials*, 2016, **107**, 102–114.

40 J. Liu, G. Zong, L. He, Y. Zhang, C. Liu and L. Wang, *Micromachines*, 2015, **6**, 855–864.

41 N. Hao, H. Yang, L. Li, L. Li and F. Tang, *New J. Chem.*, 2014, **38**, 4258–4266.

42 I. I. Slowing, J. L. Vivero-Escoto, Y. Zhao, K. Kandel, C. Peeraphatdit, B. G. Trewyn and V. S.-Y. Lin, *Small*, 2011, **7**, 1526–1532.

43 E. Carenza, V. Barceló, A. Morancho, J. Montaner, A. Rosell and A. Roig, *Acta Biomater.*, 2014, **10**, 3775–3785.

44 G. Forn-Cuní, M. Varela, C. M. Fernández-Rodríguez, A. Figueras and B. Novoa, *J. Endocrinol.*, 2015, **224**, 159–170.

45 T. Yu, D. Hubbard, A. Ray and H. Ghandehari, *J. Controlled Release*, 2012, **163**, 46–54.

46 A. L. B. De Barros, K. S. De Oliveira Ferraz, T. C. S. Dantas, G. F. Andrade, V. N. Cardoso and E. M. B. de Sousa, *Mater. Sci. Eng., C*, 2015, **56**, 181–188.

47 B. Godin, C. Chiappini, S. Srinivasan and J. F. Alexander, *Adv. Funct. Mater.*, 2012, **22**, 4225–4235.